Journal of Physics Communications

Check for updates

OPEN ACCESS

RECEIVED
2 May 2025

REVISED
5 November 2025

ACCEPTED FOR PUBLICATION
20 November 2025

PUBLISHED
2 December 2025

Original content from this work may be used under the terms of the Creative Commons Attribution 4.0 licence.

Any further distribution of this work must maintain attribution to the author(s) and the title of the work, journal citation and DOI.

PAPER

Nondipole tunneling dynamics in strong-field ionization from atomic *p* orbitals

Xiaodan Mao[1,2], **Hongcheng Ni**[1,3,*] and **Jian Wu**[1,3,4]

[1] State Key Laboratory of Precision Spectroscopy, East China Normal University, Shanghai 200241, People's Republic of China
[2] Key Laboratory for Laser Plasmas (Ministry of Education) and School of Physics and Astronomy, Collaborative Innovation Center of IFSA (CICIFSA), Shanghai Jiao Tong University, Shanghai 200240, People's Republic of China
[3] Collaborative Innovation Center of Extreme Optics, Shanxi University, Taiyuan, Shanxi 030006, People's Republic of China
[4] Chongqing Key Laboratory of Precision Optics, Chongqing Institute of East China Normal University, Chongqing 401121, People's Republic of China
[*] Author to whom any correspondence should be addressed.

E-mail: hcni@lps.ecnu.edu.cn

Keywords: nondipole effects, linear momentum, tunneling ionization, *p* orbital

Abstract

The nondipole effect breaks the symmetry of the laser field along the propagation direction, while the atomic *p* orbitals introduce distinct projections of the angular momentum along the quantization axis different from the *s* orbitals. The coupling between them gives rise to intriguing nondipole tunneling dynamics during the process of strong-field ionization. In this work, we develop a magnetic quantum number *m*-resolved nondipole saddle-point approximation method to investigate the nondipole tunneling dynamics of Ne 2*p* orbitals in strong laser fields. Our findings reveal that photoelectrons from different initial atomic orbitals display distinct dynamical behaviors both at the tunnel exit and in the asymptotic region. Specifically, the electron emitted from the orbital counterrotating to the electric field acquires a larger initial linear momentum transfer at the tunnel exit but a smaller asymptotic linear momentum transfer in the asymptotic region compared to that from the corotating orbital. Our study provides detailed insights into the nondipole tunneling dynamics of photoelectrons from different atomic orbitals in a time-resolved manner.

1. Introduction

Strong-field ionization (SFI) as a fundamental process in the interaction of atoms with intense laser fields has long attracted significant attention [1, 2]. The dipole approximation is widely used in the simulations of SFI [3], treating the laser field as uniform in space while sacrificing photon momentum details. Rare gas atoms, owing to their straightforward and stable structures, are commonly employed as experimental targets in SFI. However, for computational convenience, their numerical simulations typically assume the initial atomic orbital to be an *s*-orbital rather than a *p*-orbital [4, 5]. To fully capture the tunneling dynamics of photoelectrons from different initial atomic orbitals in strong laser fields, we need to incorporate the influence of the magnetic quantum number *m* of the initial orbitals to investigate nondipole linear momentum transfer in the laser field.

The initial atomic orbitals have a non-negligible influence on SFI. Their magnetic quantum numbers *m* characterize the angular momentum properties along the quantization axis. Bound electrons with $m = \pm 1$ exhibit either clockwise or counterclockwise motion around the nucleus [6, 7], introducing distinct projections along the quantization axis. Within the circularly polarized laser field defined in the present study, the p_+ electron corotates with the laser field, while the p_- electron counterrotates. Prior theoretical research indicates that the ionization rate of the p_- electron is markedly greater than that of the p_+ electron [8, 9], and this phenomenon has been verified experimentally [10, 11]. Moreover, the angular distributions of $p_\pm$ electrons display distinct angular distribution offsets, a finding resulting from the laser-induced deformation of the *p* orbitals [12]. Recently, a subcycle conservation law between the angular momentum and energy [13, 14] has been found and the influence of initial atomic orbitals on the conservation law has been discussed [15]. In short, electrons

© 2025 The Author(s). Published by IOP Publishing Ltd

from different initial orbitals carry distinct initial phases when ionized, leading to diverse dynamical behaviors [16–18].

Nondipole effects break the symmetry of the laser field along its propagation direction. Within the nondipole framework, the vector potential $\boldsymbol{A}(\boldsymbol{r}, t)$ is spatially dependent. Due to radiation pressure and magnetic field effects [19, 20], the photoelectron momentum distribution exhibits a nonzero shift along the propagation direction of the laser field during SFI, which represents a typical signature of nondipole effects. With the improvement in experimental detection precision, the observation of this weak nondipole effects has become possible. In 2011, the linear momentum transfer along the laser propagation direction was experimentally observed during the SFI of Ar and Ne atoms using circularly polarized laser pulses [21]. Subsequently, the SFI experiment of Xe atoms using linearly polarized laser fields revealed a linear momentum transfer in the opposite direction, a phenomenon attributed to the interplay between the magnetic field and Coulomb potential [22]. To enhance measurement precision, an experimental scheme employed two counterpropagating laser pulses that form a standing wave to ionize Ar atoms, accurately determining the zero point of the momentum distribution [23], thereby confirming the theoretical predictions of linear momentum transfer [24, 25]. Remarkably, the nondipole linear momentum transfer is manifested in both single-photon ionization [26–28] and tunneling ionization [29–31], where the effects of electric quadrupole and magnetic dipole interactions can be individually identified. Additionally, during the under-barrier motion in tunneling ionization, the Coulomb potential significantly influences the linear momentum transfer [32, 33]. In above-threshold ionization (ATI), nondipole effects induce a shift of $-U_p/c$ to the center of the ATI momentum rings along the laser propagation direction [34–38], where U_p represents the ponderomotive energy and c is the speed of light. This phenomenon has been experimentally observed [39]. In 2019, the experimental observation of linear momentum transfer on the subcycle timescale was achieved [40] using the attoclock protocol [41, 42]. These findings were soon followed by advancements in corresponding theoretical frameworks [43, 44]. Recently, the RABBIT [45] technique has been employed to experimentally capture the electron subcycle motion along the laser propagation direction in He atoms, as well as the time delay between electric dipole and electric quadrupole transitions [46]. Overall, the linear momentum transfer phenomenon induced by nondipole effects is present in a wide range of SFI processes [47–52].

SFI is a two-stage process including quantum tunneling and the subsequent classical continuum motion. By examining the behavior of electrons at the tunnel exit and in the asymptotic region, their dynamics during these two stages in intense laser fields can be characterized. Along the laser field propagation direction ($\hat{\boldsymbol{e}}_z$), the linear momentum transfer can be correspondingly decomposed into two components [43, 53]:

$$\langle p_z \rangle = \langle v_z \rangle + \frac{\Delta E}{c}, \tag{1}$$

where $\langle v_z \rangle$ and $\langle p_z \rangle$ represent the average linear momentum transfer at the tunnel exit and in the asymptotic region, respectively, and ΔE denotes the energy accumulated by the electron during the continuum motion.

In this study, we focus on the SFI of the $2p$ orbitals of Ne in strong laser fields. For analyzing the nondipole tunneling dynamics of photoelectrons originating from those orbitals at the tunnel exit and in the asymptotic regime, we propose a magnetic quantum number m-resolved nondipole saddle-point approximation (m-ndSPA) method. It successfully reproduces most of the results obtained from solving the time-dependent Schrödinger equation (TDSE) and the backpropagation method [2, 54–56]. This includes the distributions of the initial transverse momentum $v_\perp$, energy E_0, and position r_0 at the tunnel exit, as well as the asymptotic radial momentum $p_\perp$ and energy $E_\perp$ distributions, and the linear momentum transfer $\langle p_z \rangle$ in the asymptotic region. However, the current m-ndSPA method fails to capture the order of the linear momentum transfer $\langle v_z \rangle$ for $p_\pm$ electrons at the tunnel exit. We anticipate the development of a more comprehensive m-ndSPA method in the future. In our numerical simulations, we systematically investigate the cases of strong circularly polarized (CP), elliptically polarized (EP), and two-color (TC) circularly polarized laser fields, including corotating (CoRTC) and counterrotating (CRTC) cases.

The article is organized as follows. In section 2, we introduce the theoretical methods employed in this study, including the TDSE, backpropagation, and m-ndSPA methods. In section 3, we explore the nondipole tunneling dynamics of $p_\pm$ electrons at the tunnel exit in the CP, EP, and TC fields. In section 4, we discuss the nondipole tunneling dynamics of $p_\pm$ electrons in the asymptotic region. The conclusions are given in section 5. Atomic units are used throughout unless noted otherwise.

2. Theoretical framework

In this section, we briefly introduce the theoretical methods for investigating the ionization dynamics of Ne atoms with initial $2p$ orbitals in strong laser fields, including the TDSE, backpropagation, and m-ndSPA

methods. In the numerical simulations, we employ CP and EP fields with a vector potential of

$$\boldsymbol{A}(t) = A_0 \cos(\omega t)\hat{\boldsymbol{e}}_x + \epsilon A_0 \sin(\omega t)\hat{\boldsymbol{e}}_y, \tag{2}$$

where the peak laser intensity $I_0 = 5 \times 10^{14}$ W cm^{-2}, the wavelength $\lambda = 800$ nm, and the ellipticity $\epsilon = 1$ for CP field and $\epsilon = 0.7$ for EP field, as well as TC fields with a vector potential expressed as

$$\begin{aligned} \boldsymbol{A}_{\mathrm{TC}}(t) &= A_0\left[\cos(\omega t) + \frac{\eta_{\mathrm{F}}}{2}\cos(2\omega t)\right]\hat{\boldsymbol{e}}_x \\ &\quad + A_0\left[\sin(\omega t) + \epsilon\frac{\eta_{\mathrm{F}}}{2}\sin(2\omega t)\right]\hat{\boldsymbol{e}}_y, \end{aligned} \tag{3}$$

where the peak laser intensity $I_0 = 6 \times 10^{14}$ W cm^{-2}, the fundamental wavelength $\lambda = 800$ nm, the ellipticity $\epsilon = \pm 1$ ($\epsilon = 1$ for CoRTC field and $\epsilon = -1$ for CRTC field), and the field amplitude ratio $\eta_{\mathrm{F}} = 0.1$. The corresponding electric field is defined as $\boldsymbol{F} = -\dot{\boldsymbol{A}}$. For these laser pulses, the temporal envelope of the vector potential is $\cos^4(\omega t/2N)$ with $N = 10$ cycles in total.

2.1. Time-dependent Schrödinger equation

We solve the three-dimensional TDSE within the single-active-electron approximation to simulate the interaction between Ne atoms with $2p$ orbitals and strong laser fields. The nondipole Hamiltonian is given as

$$H = \frac{1}{2}[\boldsymbol{p} + \boldsymbol{A}(\eta)]^2 + V(\boldsymbol{r}), \tag{4}$$

where the vector potential of the laser field $\boldsymbol{A}(\eta) = \boldsymbol{A}(t - z/c)$. We perform an expansion of the vector potential up to order c^{-1}:

$$\boldsymbol{A}(\eta) \approx \boldsymbol{A}(t) - \frac{z}{c}\dot{\boldsymbol{A}}(t) = \boldsymbol{A}(t) + \frac{z}{c}\boldsymbol{F}(t). \tag{5}$$

Substitution into equation (4) yields

$$H = \frac{1}{2}[\boldsymbol{p} + \boldsymbol{A}(t)]^2 + \frac{z}{c}[\boldsymbol{p} + \boldsymbol{A}(t)] \cdot \boldsymbol{F}(t) + V(\boldsymbol{r}). \tag{6}$$

Through gauge transformation, the Hamiltonian becomes [23, 29, 43, 47]

$$\begin{aligned} H &= \frac{1}{2}\left[\boldsymbol{p} + \boldsymbol{A}(t) + \frac{\hat{\boldsymbol{e}}_z}{c}\left(\boldsymbol{p}\cdot\boldsymbol{A}(t) + \frac{A^2(t)}{2}\right)\right]^2 \\ &\quad + V\left(\boldsymbol{r} - \frac{z}{c}\boldsymbol{A}(t)\right) \end{aligned} \tag{7}$$

with the Coulomb potential

$$V(r) = -\frac{1 + 9e^{-0.85r^{1.6}}}{\sqrt{r^2 + a_0}}. \tag{8}$$

This model potential preserves the main characteristics of Ne atoms, with the electron experiencing a charge of 10 at $r = 0$ and an asymptotic charge of 1 in the long-range region. The soft-core parameter $a_0 = 1.4253$ is adjusted to ensure the atomic ionization energy $I_p = 0.7935$, representing the energy required to remove the outermost electron, matches the experimental value. The orthogonal normalized eigenfunctions $\psi_{2p_x}(\boldsymbol{r})$ and $\psi_{2p_y}(\boldsymbol{r})$ are obtained through the imaginary-time propagation method, representing the $2p_x$ and $2p_y$ orbitals of Ne, respectively. A linear combination of them yields the initial wave function

$$\psi_{\pm}(\boldsymbol{r}) = \frac{1}{\sqrt{2}}[\psi_{2p_x}(\boldsymbol{r}) \pm i\psi_{2p_y}(\boldsymbol{r})], \tag{9}$$

where the subscript $\pm$ corresponds to the magnetic quantum number $m = \pm 1$.

The time evolution of the wave function in the laser field is computed using the split-operator Fourier method. Each dimension of the computational grid consists of 1024 spatial grid points and a spatial step of $\Delta x = \Delta y = \Delta z = 0.35$ a.u., with a time step of $\Delta t = 0.02$ a.u. When the wave function approaches the grid boundaries, an absorbing function $1/[1 + \exp\{(r - r_0)/d\}]$ is employed to prevent reflections, with absorption performed every 0.2 a.u. in time, where the radius parameter $r_0 = 164.2$ a.u. and the width parameter $d = 4$ a.u. By projecting the absorbed wave function onto the nondipole Volkov state [57, 58], we obtain the

asymptotic photoelectron momentum distribution $W_{\rm TDSE}(\boldsymbol{p})$. We have verified the convergence of the calculation results with respect to the above parameters. The final average linear momentum of the photoelectrons is evaluated using

$$\langle p_z \rangle = \frac{\int W(\boldsymbol{p}) p_z d\boldsymbol{p}}{\int W(\boldsymbol{p}) d\boldsymbol{p}}, \tag{10}$$

where the ionization rate $W(\boldsymbol{p}) = W_{\rm TDSE}(\boldsymbol{p})$.

2.2. The backpropagation method

We employ a hybrid quantum–classical backpropagation method [2, 54–56] to extract the dynamical features of the electrons from p orbitals at the tunnel exit. This method is widely applied in various studies within the SFI domain, including research on tunneling time [33, 55], p-orbital tunneling [59, 60] and deformation dynamics [12], backward rescattering times [61], conservation law between the angular momentum and energy [13, 14], and nondipole effects [43]. The key to this method is the transformation of the ionized electron wave packet into classical trajectories, followed by their backpropagation along the time axis until reaching the tunnel exit. The ionized electron wave packet is obtained from quantum forward propagation using TDSE.

In the calculations, we distribute 6000 virtual detectors uniformly on a spherical shell with a radius of $r_d = 40$ a.u. to collect the electron wave packets reaching r_d and convert them into classical trajectories. These trajectories are backpropagated along the time axis until the tunnel exit, following Newton's equation of motion. During the backward propagation, the tunnel exit is identified when the momentum of a classical trajectory along the instantaneous electric field direction vanishes. The convergence of the calculation results with respect to the numerical parameters has been tested.

2.3. *m*-resolved nondipole saddle-point approximation

To gain deeper insights into the ionization dynamics of Ne $p_\pm$ orbitals, we develop a magnetic quantum number m-resolved nondipole saddle-point approximation method (m-ndSPA). Within the nondipole strong-field approximation (ndSFA) framework, both the effect of the laser field on the initial bound state and the Coulomb interaction on the final continuum state are ignored. Based on the nondipole Hamiltonian [equation (4)], the transition amplitude in the length gauge (LG) is given as [32, 57]

$$M_{\pm}^{\rm ndSFA}(\boldsymbol{p}) = -i \int_{-\infty}^{\infty} d\eta \left[\left(1 - \frac{p_z}{c}\right) i \boldsymbol{\nabla}_{\boldsymbol{k}} \tilde{\psi}_{\pm}(\boldsymbol{k}) \cdot \boldsymbol{F}(\eta) e^{iS(\eta)} \right], \tag{11}$$

where $\boldsymbol{k} = \boldsymbol{p} + \boldsymbol{A}(\eta) - (E + I_p)\hat{\boldsymbol{e}}_z/c$, the nondipole phase

$$S(\eta) = \int^{\eta} dt \left\{ \frac{1}{2}p^2 + \frac{\boldsymbol{p} \cdot \boldsymbol{A}(t) + A^2(t)/2}{(1 - p_z/c)} + I_p \right\}, \tag{12}$$

and the Fourier transform of the initial-state wave function $\tilde{\psi}_{\pm}(\boldsymbol{k}) = \int d\boldsymbol{r} \exp(-i\boldsymbol{k} \cdot \boldsymbol{r}) \psi_{\pm}(\boldsymbol{r})$. The asymptotic form of the initial wave function in the momentum space is given as [62, 63]

$$\begin{aligned} \tilde{\psi}_{\pm}(\boldsymbol{k}) \;=\; & \frac{A(-ik)^l}{2^{l+1/2}(2I_p)^{(l-\nu)/2}} \frac{\Gamma(l+\nu+2)}{\Gamma(l+3/2)} \\ & \times {}_2F_1\left(\frac{l-\nu}{2}, \frac{l-\nu+1}{2}, l+\frac{3}{2}; -\frac{k^2}{2I_p}\right) \frac{Y_{lm}(\hat{\boldsymbol{k}})}{(k^2+2I_p)^{\nu+1}}, \end{aligned} \tag{13}$$

with $l = 1$, $m = \pm 1$, $\nu = 1/\sqrt{2I_p}$, the gamma function $\Gamma(x)$, the spherical harmonics Y_{lm}, and the Gauss hypergeometric function ${}_2F_1(a, b, c; z)$. For the valence shell of Ne, $A = 2.1$ [63].

To facilitate calculations, we ignore dynamics-independent prefactors and consider an approximate form of equation (13) [15]:

$$\tilde{\psi}_{\pm}(\boldsymbol{k}) \simeq \frac{k_x + imk_y}{(k^2 + 2I_p)^{\nu+1}}. \quad (m = \pm 1) \tag{14}$$

By substituting this wave function into equation (11), the expression can be reformulated as

$$M_{\pm}^{\rm ndSFA}(\boldsymbol{p}) = \int_{-\infty}^{\infty} d\eta \left(1 - \frac{p_z}{c}\right) f(\eta) e^{iS(\eta)}, \tag{15}$$

where

$$\begin{aligned} f(\eta) &= \frac{\partial}{\partial \boldsymbol{k}}\left[\frac{k_x + imk_y}{(k^2 + 2I_p)^{\nu+1}}\right] \cdot \boldsymbol{F}(\eta) \\ &= \frac{1}{(k^2 + 2I_p)^{\nu+2}}[(F_x + imF_y)(2I_p + k_z^2 - \nu k_\perp^2) \\ &\quad +(-F_x + imF_y)(1+\nu)(k_x + imk_y)^2]. \end{aligned} \tag{16}$$

To include the impact of the magnetic quantum number m on the saddle-point equation (SPE), we reformulate $f(\eta)$ as

$$f(\eta) = f_m(\eta) e^{im\phi_F} \tag{17}$$

with

$$\begin{aligned} f_m(\eta) &= \frac{-imF(\eta)}{(k^2 + 2I_p)^{\nu+2}}[2I_p + k_z^2 - \nu k_\perp^2 \\ &\quad + (1+\nu)(k_x + imk_y)^2 e^{-2im\phi_F}], \end{aligned} \tag{18}$$

$F(\eta) = \sqrt{F_x^2(\eta) + F_y^2(\eta)}$, and

$$\phi_F = \arctan\left(\frac{F_x(\eta)}{-F_y(\eta)}\right), \tag{19}$$

where applying

$$F_x(\eta) + imF_y(\eta) = -imF(\eta)e^{im\phi_F}, \quad (m = \pm 1) \tag{20}$$

$$-F_x(\eta) + imF_y(\eta) = -imF(\eta)e^{-im\phi_F}. \quad (m = \pm 1) \tag{21}$$

Thus, the two exponential terms in equation (15) can be combined into one

$$e^{iS_m(\eta)} = e^{im\phi_F} e^{iS(\eta)}, \tag{22}$$

where $S_m(\eta) = S(\eta) + m\phi_F$. The term $f_m(\eta)$ remains slowly varying relative to the action term $S_m(\eta)$ at the saddle point. Therefore, we can apply the saddle-point approximation [62, 63]

$$\int_C e^{iS(z)} dz \approx \sum_j \sqrt{2\pi i}\,(\ddot{S})^{-1/2} e^{iS(z_j)} \tag{23}$$

to calculate equation (15), giving

$$M_\pm^{m\text{-ndSPA}}(\boldsymbol{p}) \approx \sum_{\eta_s}\left(1 - \frac{p_z}{c}\right) f_m(\eta_s)[\ddot{S}_m(\eta_s)]^{-1/2} e^{iS_m(\eta_s)} \tag{24}$$

with the complex saddle-point time $\eta_s = \eta_r + i\eta_i$. The ionization time is represented by the real part of the saddle-point time η_r, and the imaginary part η_i relates to the tunneling ionization rate. It is obtained by solving the m-resolved nondipole saddle-point equation (m-ndSPE):

$$-\dot{S}_m = \frac{p^2}{2} + \left(1 + \frac{p_z}{c}\right)\left[\boldsymbol{p} \cdot \boldsymbol{A}(\eta_s) + \frac{1}{2}A^2(\eta_s)\right] + I_p + m\dot{\phi}_F = 0, \tag{25}$$

where the phase derivative

$$\dot{\phi}_F = \frac{\epsilon\omega}{\epsilon^2 \cos^2(\omega\eta) + \sin^2(\omega\eta)} \tag{26}$$

for CP and EP fields, and

$$\dot{\phi}_F = \frac{2 + 4\eta_F^2\epsilon + 3\eta_F(1+\epsilon)\cos(\omega\eta) + \eta_F(1-\epsilon)\cos(3\omega\eta)}{2[1 + \eta_F^2 + \eta_F(1+\epsilon)\cos(\omega\eta) - \eta_F(1-\epsilon)\cos(3\omega\eta)]}\omega \tag{27}$$

for TC fields. In CP fields, $\dot{\phi}_F = \epsilon\omega$ with $\epsilon = \pm 1$. For EP and TC fields, we approximate $\dot{\phi}_F$ by its value at the peak time of the respective laser electric field, resulting in $\dot{\phi}_F \approx \epsilon\omega$ for EP fields and $\dot{\phi}_F \approx \omega(1 + 2\epsilon\eta_F)/(1 + \eta_F)$ for TC fields. Key parameters at the peak laser electric field are summarized in table 1.

Table 1. Key parameters when the electric field reaches its maximum value in different laser fields: the time η_0, electric field F, vector potential A, and the phase derivative $\dot{\phi}_F$.

Field	η_0	$F(\eta_0)$	$A(\eta_0)$	$\dot{\phi}_F(\eta_0)$
CP ($\epsilon=1$) EP ($\epsilon=0.7$)	all $\frac{\pi}{2\omega}$	$A_0\omega$	ϵA_0	$\epsilon\omega$
CoRTC ($\epsilon=1$) CRTC ($\epsilon=-1$)	0 $\frac{\pi}{\omega}$	$(1+\eta_F)A_0\omega$	$(1+\epsilon\frac{\eta_F}{2})A_0$	$\frac{1+2\epsilon\eta_F}{1+\eta_F}\omega$

Since we approximate $\dot{\phi}_F$ by its value at the peak time of the laser field, the m-ndSPE can be rewritten as

$$\frac{p^2}{2}+\left(1+\frac{p_z}{c}\right)\left[\boldsymbol{p}\cdot\boldsymbol{A}(\eta_s)+\frac{1}{2}A^2(\eta_s)\right]+I_p'=0, \tag{28}$$

where $I_p'=I_p+m\dot{\phi}_F$ is η_s-independent. The complex vector potential is separated into real and imaginary components:

$$\boldsymbol{A}(\eta_s)=\mathrm{Re}\,\boldsymbol{A}(\eta_s)+i\,\mathrm{Im}\,\boldsymbol{A}(\eta_s). \tag{29}$$

Substitution into equation (28) yields the imaginary part of the the m-ndSPE

$$i\left(1+\frac{p_z}{c}\right)\{[\boldsymbol{p}_\perp+\mathrm{Re}\,\boldsymbol{A}(\eta_s)]\cdot\mathrm{Im}\,\boldsymbol{A}(\eta_s)\}=0 \tag{30}$$

with the component of $\boldsymbol{p}$ in the laser polarization plane $\boldsymbol{p}_\perp=(p_x,p_y)$. Since $\boldsymbol{p}_\perp+\mathrm{Re}\,\boldsymbol{A}(\eta_s)$ is perpendicular to $\mathrm{Im}\,\boldsymbol{A}(\eta_s)=(\mathrm{Im}\,A_x(\eta_s),\ \mathrm{Im}\,A_y(\eta_s))$, the unit vector representing its direction is

$$\hat{\boldsymbol{k}}_\perp=\frac{-\mathrm{Im}A_y(\eta_s)\hat{\boldsymbol{e}}_x+\mathrm{Im}A_x(\eta_s)\hat{\boldsymbol{e}}_y}{\sqrt{[\mathrm{Im}A_x(\eta_s)]^2+[\mathrm{Im}A_y(\eta_s)]^2}}. \tag{31}$$

Thus, by defining the auxiliary momentum as

$$k_\perp=[\boldsymbol{p}+\mathrm{Re}\,\boldsymbol{A}(\eta_s)]\cdot\frac{-\mathrm{Im}A_y(\eta_s)\hat{\boldsymbol{e}}_x+\mathrm{Im}A_x(\eta_s)\hat{\boldsymbol{e}}_y}{\sqrt{[\mathrm{Im}A_x(\eta_s)]^2+[\mathrm{Im}A_y(\eta_s)]^2}}, \tag{32}$$

Equation (30) is fulfilled automatically. This approach confines the search for saddle points to a single axis, substantially reducing computational complexity compared to the traditional full complex-plane exploration [29, 44, 64]. Moreover, as the computations are conducted within the $(\eta_r, k_\perp, p_z)$ coordinate system, it is necessary to account for the Jacobian factor of the coordinate transformation in the ionization rate calculation:

$$W_\pm^{m\text{-ndSPA}}(\eta_r,k_\perp,p_z)=\left|\det\frac{\partial(p_x,p_y,p_z)}{\partial(\eta_r,k_\perp,p_z)}\right||M_\pm^{m\text{-ndSPA}}(\boldsymbol{p})|^2. \tag{33}$$

The asymptotic average linear momentum transfer is then calculated by substituting it into equation (10).

From the conservation of (p_z-E/c) in the Hamiltonian [equation (4)] with the Coulomb potential neglected, we obtain the relationship between the initial and asymptotic linear momentum transfer: $v_z=p_z+\frac{1}{c}\left[\boldsymbol{p}\cdot\boldsymbol{A}(\eta)+\frac{1}{2}A^2(\eta)\right]$. Since $z\approx0$ during the tunneling process implies $\eta_r\approx t_r$, the average linear momentum transfer $\langle v_z\rangle$ as a function of the ionization time t_r is given as

$$\langle v_z(t_r)\rangle=\langle v_z(\eta_r)\rangle=\frac{\int W_\pm^{m\text{-ndSPA}}(\eta_r,k_\perp,p_z)v_z\,dk_\perp dp_z}{\int W_\pm^{m\text{-ndSPA}}(\eta_r,k_\perp,p_z)\,dk_\perp dp_z}. \tag{34}$$

3. The tunneling region

In this section, we investigate the tunneling dynamics of Ne $p_\pm$ orbitals at the tunnel exit under the influence of intense CP, EP, and TC laser fields. The validity of our m-ndSPA method is confirmed through comparison with the backpropagation method, yielding generally consistent conclusions. The first step of the back-propagation method is based on the fully quantum propagation of the ionized wave packet, ensuring optimal preservation of photoelectron dynamics information and thereby supporting the extraction of precise tunneling exit characteristics.

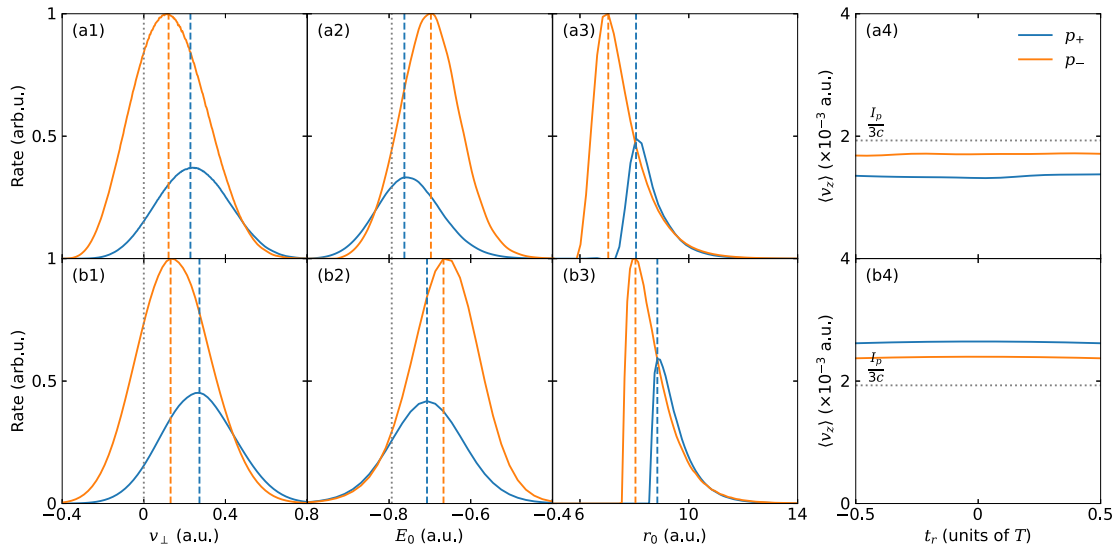

Figure 1. The distributions of initial transverse momentum [column (1)], energy [column (2)], position [column (3)], and the subcycle time-resolved linear momentum $\langle v_z \rangle(t_r)$ [column (4)] at the tunnel exit for photoelectrons ionized from $p_\pm$ orbitals of Ne in the CP field, calculated by the backpropagation [row (a)] and m-ndSPA [row (b)] methods. The blue and orange solid lines denote the p_+ and p_- orbitals, respectively, with vertical dashed lines marking the peak positions of their respective distributions. The gray dotted lines mark the positions of $v_\perp = 0$, $E_0 = -I_p$, and $\langle v_z \rangle = I_p/(3c)$.

In figure 1 we compare the tunneling exit characteristics of $p_\pm$ photoelectrons in a CP field, obtained using the backpropagation [row (a)] and m-ndSPA [row (b)] methods. These include the distributions of initial transverse momentum [column (1)], energy [column (2)], position [column (3)], as well as the subcycle time-resolved linear momentum [column (4)] at the tunnel exit.

The findings presented in figures 1(a1)–(a3) indicate that the p_- electron (counterrotating to the CP field) is more easily ionized compared to the p_+ electron (corotating to the CP field), in agreement with earlier investigations [8, 9]. The initial energy is calculated as

$$E_0 = \frac{1}{2}(v_\perp^2 + v_z^2) + \boldsymbol{r}_0 \cdot \boldsymbol{F}, \tag{35}$$

where $v_\perp$ and v_z denote the momentum components in the polarization plane and along the propagation direction of the laser field, respectively. Despite the larger initial transverse momentum of the p_+ electron compared to the p_- electron, its initial energy E_0 is lower due to its initial position being farther from the nucleus. At the tunnel exit, the influence of the tunneling exit position on energy is greater than that of the initial transverse momentum. A comparison between figures 1(a) and (b) indicates that the initial transverse momentum, energy, and position derived from the two methods exhibit discrepancies. These differences arise from the Coulomb interaction, which is not included in the m-ndSPA method but is considered within the backpropagation method. The initial transverse momentum could be obtained more accurately by including under-barrier Coulomb corrections [32]. A more significant discrepancy resides in the tunneling exit position, which is also the primary source leading to the discrepancy in the tunneling energy. A possible remedy is to incorporate an adiabatic correction to the exit position $r_0^{\rm ad} \approx (I_p + \sqrt{I_p^2 - 4F})/2F \approx I_p/F - 1/I_p$ so that $\Delta r_0 \approx -1/I_p$.

We now analyze the subcycle time-resolved linear momentum characteristics of $p_\pm$ electrons at the tunnel exit, by comparing the initial average momentum transfer $\langle v_z(t_r) \rangle$ from the backpropagation method with that from the m-ndSPA method, presented in figure 1(4). According to the backpropagation method, the p_+ electron displays lower linear momentum transfer at the tunnel exit than the p_- electron, as illustrated in figure 1(a4). However, the m-ndSPA method leads to the opposite conclusion, as shown in figure 1(b4). As a comparison, for the s electron, the average linear momentum transfer at the tunnel exit is given as [43]

$$\langle v_z \rangle \approx \frac{2I_p + \langle v_\perp^2 \rangle}{6c}\left[1 - \frac{2\alpha_Z F}{(2I_p)^{3/2}}\right], \tag{36}$$

where $\alpha_Z = 1 + 1/\sqrt{2I_p}$ and $\langle v_\perp^2 \rangle \approx \langle v_\perp \rangle^2 + F/(2\sqrt{2I_p})$. Clearly, the average initial transverse momentum $\langle v_\perp \rangle$ has a positive effect on $\langle v_z \rangle$. However, as shown in figure 1(a), although $\langle v_\perp \rangle_+ > \langle v_\perp \rangle_-$, we have $\langle v_z \rangle_+ < \langle v_z \rangle_-$, indicating that $\langle v_\perp \rangle$ negatively affects $\langle v_z \rangle$ for $p_\pm$ electrons. Apparently, unknown physical effects are at play here, which is beyond the framework governing equation (36) for s orbitals, that leads to the reverse

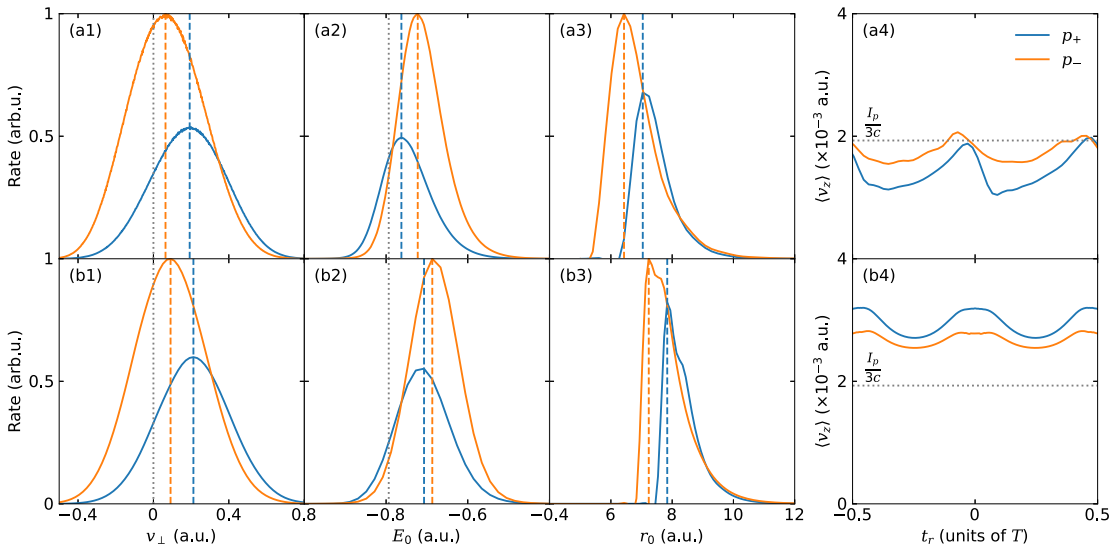

Figure 2. Same as figure 1 but for the EP field with an ellipticity $\epsilon = 0.7$.

order in $\langle v_z \rangle$ for $p_\pm$ orbitals. We have attempted to incorporate m-dependent Coulomb correction to the under-barrier tunneling process [32] as well as orbital deformation of the $p_\pm$ orbitals [12], but these efforts failed to reproduce the observation from the backpropagation method. We expect the formulation of an improved m-ndSPA method, e.g., by including excited states, to accurately capture this feature in the future, which goes beyond the scope of the present work.

We now examine the tunneling dynamics of $p_\pm$ electrons in a EP laser field. Figure 2 presents the information of photoelectrons at the tunnel exit, as obtained through the backpropagation and m-ndSPA methods. Consistent with the findings in the CP field, the p_- electron exhibits higher ionization rate and is released from the position closer to the nucleus compared to the p_+ electron. At the tunnel exit, the p_- electron has greater initial energy but lower initial transverse momentum. These characteristics are observed in both the backpropagation and m-ndSPA methods. In terms of the initial linear momentum transfer, the backpropagation method reveals that $\langle v_z \rangle_+ < \langle v_z \rangle_-$, a result that the m-ndSPA method fails to reproduce. Nonetheless, the 2ω subcycle oscillation of $\langle v_z \rangle$ is fully captured by the m-ndSPA method, as shown in figure 2(b4). The underlying physical mechanism governing the subcycle modulation in $\langle v_z \rangle$ is obvious from equation (36). Apart from the coefficient $[1 - 2\alpha_Z F/(2I_p)^{3/2}]$ present due to the initial-state distribution, the modulation in $\langle v_z \rangle$ is due to the existence of the initial transverse momentum $v_\perp$ which varies on the subcycle level due to nonadiabatic effects. Therefore, it is the interplay between nonadiabatic and nondipole effects that leads to the subcycle modulation in $\langle v_z \rangle$ [43, 44].

Let us turn our attention to the TC field. In figure 3, the computational results obtained by the backpropagation and m-ndSPA methods are displayed, respectively. Given the fact that η_F has a small value ($\eta_F = 0.1$), the fundamental wave dominates both CoRTC and CRTC fields, hence the p_+ orbital largely corotates with both CoRTC and CRTC fields, we can thus reach the similar conclusions: (1) the p_- electron exhibits higher ionization rate than the p_+ electron; (2) Compared to the p_- electron, the p_+ electron has larger initial transverse momentum and initial position but lower initial energy at the tunnel exit.

Figure 3(4) illustrates the characteristics of linear momentum transfer for $p_\pm$ electrons in the TC field. Consistent with the findings in the CP and EP fields, the backpropagation method confirms that p_- electron possess larger linear momentum transfer. Similarly, the m-ndSPA method still exhibits limitations when extracting the order of $\langle v_z \rangle$ for $p_\pm$ orbitals in the TC field, albeit successfully capturing the subcycle modulations.

4. The asymptotic region

In this section, we investigate the tunneling dynamics of Ne $p_\pm$ orbitals in the asymptotic region under the influence of intense CP, EP, and TC laser fields. Both the TDSE and m-ndSPA methods are employed in the calculations, yielding consistent results.

In figure 4 we present a comparison of the asymptotic $p_\pm$ photoelectron characteristics in the CP field as calculated by the TDSE [row (a)] and m-ndSPA [row (b)] methods: the distributions of asymptotic radial momentum [column (1)], energy [column (2)], as well as the linear momentum transfer $\langle p_z \rangle$ as a function of the attoclock angle $\phi_p = \arctan(p_y/p_x)$ [column (3)] in the asymptotic region.

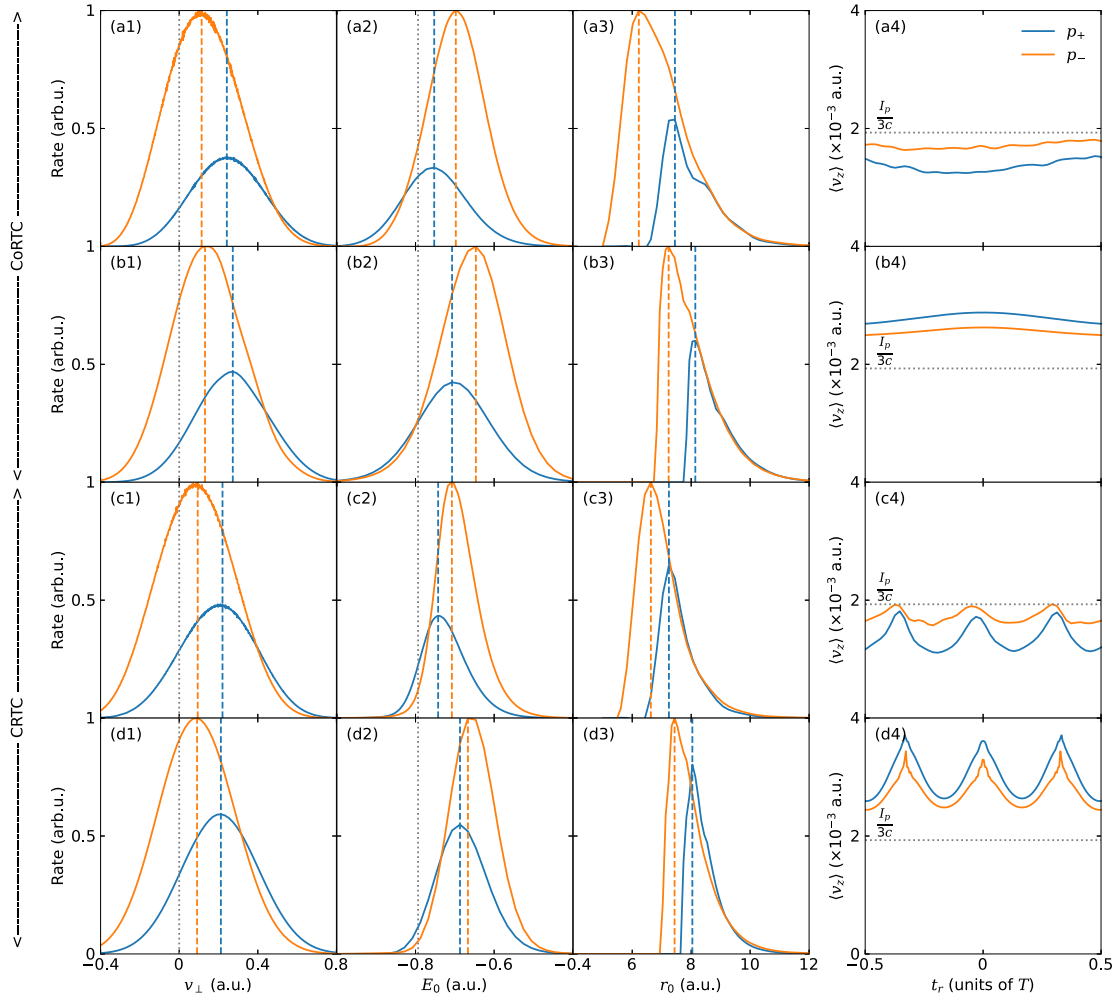

Figure 3. Same as figure 1 but for the CoRTC [the upper two rows (a) and (b)] and CRTC [the lower two rows (c) and (d)] fields. The results displayed in rows (a) and (c) are obtained from the backpropagation method, whereas those in rows (b) and (d) are computed using the m-ndSPA method.

The results in figures 4(a1),(a2) show that the p_+ electron has larger asymptotic radial momentum $p_\perp$ and energy $E = p^2/2$ than the p_- electron. The asymptotic radial momentum is given by

$$\boldsymbol{p}_\perp = \boldsymbol{v}_\perp - \boldsymbol{A} + \Delta\boldsymbol{p}_\perp, \tag{37}$$

where $\Delta\boldsymbol{p}_\perp$ is the momentum shift indued by the Coulomb interaction. In the CP field, $\langle v_\perp \rangle_+ > \langle v_\perp \rangle_-$, leading to the conclusion that $\langle p_\perp \rangle_+ > \langle p_\perp \rangle_-$. The difference in asymptotic radial momentum in figures 4(a1),(a2) and (b1),(b2) is attributed to the $\Delta\boldsymbol{p}_\perp$ term. In the m-ndSPA method, $\Delta\boldsymbol{p}_\perp = 0$, since Coulomb interaction is neglected. To account for the Coulomb interaction, trajectory-based Monte Carlo simulations could be performed, starting from the initial tunneling exit conditions and incorporating the full Coulomb potential during the continuum propagation.

The results of the linear momentum transfer $\langle p_z \rangle$ for $p_\pm$ electrons in the asymptotic region are shown in figure 4(a3). The results indicate that the p_+ electron gains higher $\langle p_z \rangle$ than the p_- electron. $\langle p_z \rangle$ in the asymptotic region originates from the accumulation of linear momentum during both the tunneling process and the subsequent continuum motion [equation (1)]. $\langle p_z \rangle$ is primarily contributed by the continuum motion, during which coupling to the vector potential magnifies the contribution of the initial transverse momentum $\boldsymbol{v}_\perp$:

$$\begin{aligned} \frac{\Delta E}{c} &= \frac{\langle p_\perp^2 \rangle - \langle v_\perp^2 \rangle}{2c} \\ &= \frac{\langle (\boldsymbol{v}_\perp - \boldsymbol{A})^2 \rangle - \langle v_\perp^2 \rangle}{2c} = \frac{-2\langle \boldsymbol{v}_\perp \rangle \cdot \boldsymbol{A} + A^2}{2c} \\ &\approx \frac{2\langle v_\perp \rangle A + A^2}{2c}. \end{aligned} \tag{38}$$

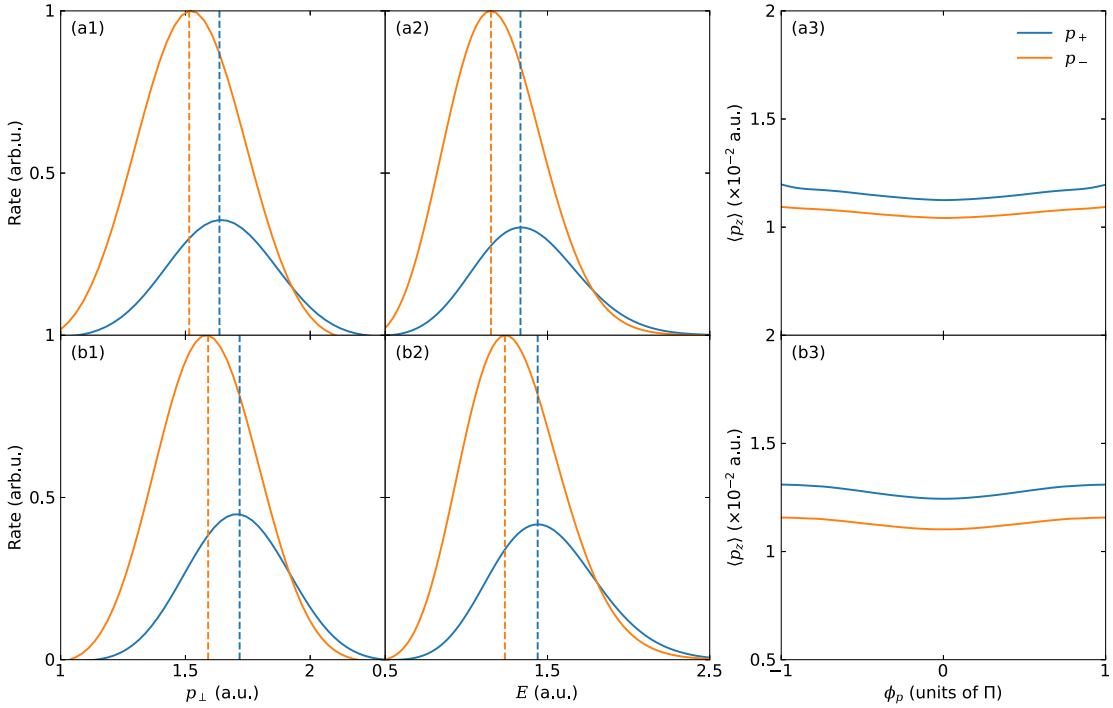

Figure 4. The distributions of asymptotic radial momentum [column (1)], energy [column (2)], and the linear momentum transfer $\langle p_z \rangle$ as a function of the attoclock angle ϕ_p [column (3)] in the asymptotic region for photoelectrons ionized from $p_\pm$ orbitals of Ne in the CP field, calculated by TDSE [row (a)] and m-ndSPA [row (b)] methods. The blue and orange solid lines denote the p_+ and p_- orbitals, respectively, with vertical dashed lines marking the peak positions of their respective distributions.

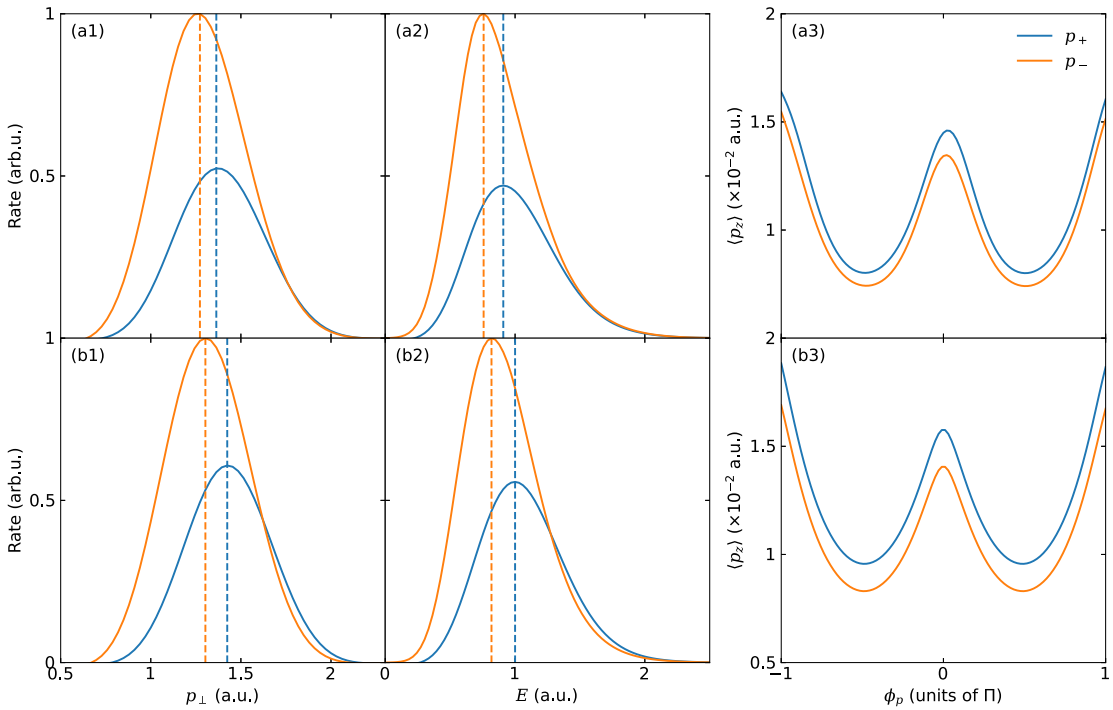

Figure 5. Same as figure 4 but for the EP field with an ellipticity $\epsilon = 0.7$.

The last expression is attributed to the fact that $\langle \boldsymbol{v}_\perp \rangle$ at the tunnel exit is oriented approximately antiparallel to the instantaneous vector potential $\boldsymbol{A}$ in the CP field. Since $\langle v_\perp \rangle_+ > \langle v_\perp \rangle_-$ [figure 1(1)], it follows that $\langle p_z \rangle_+ > \langle p_z \rangle_-$. According to this expression, the subcycle modulation in the asymptotic linear momentum transfer $\langle p_z \rangle$ arises primarily from corresponding variations in the magnitude of the vector potential.

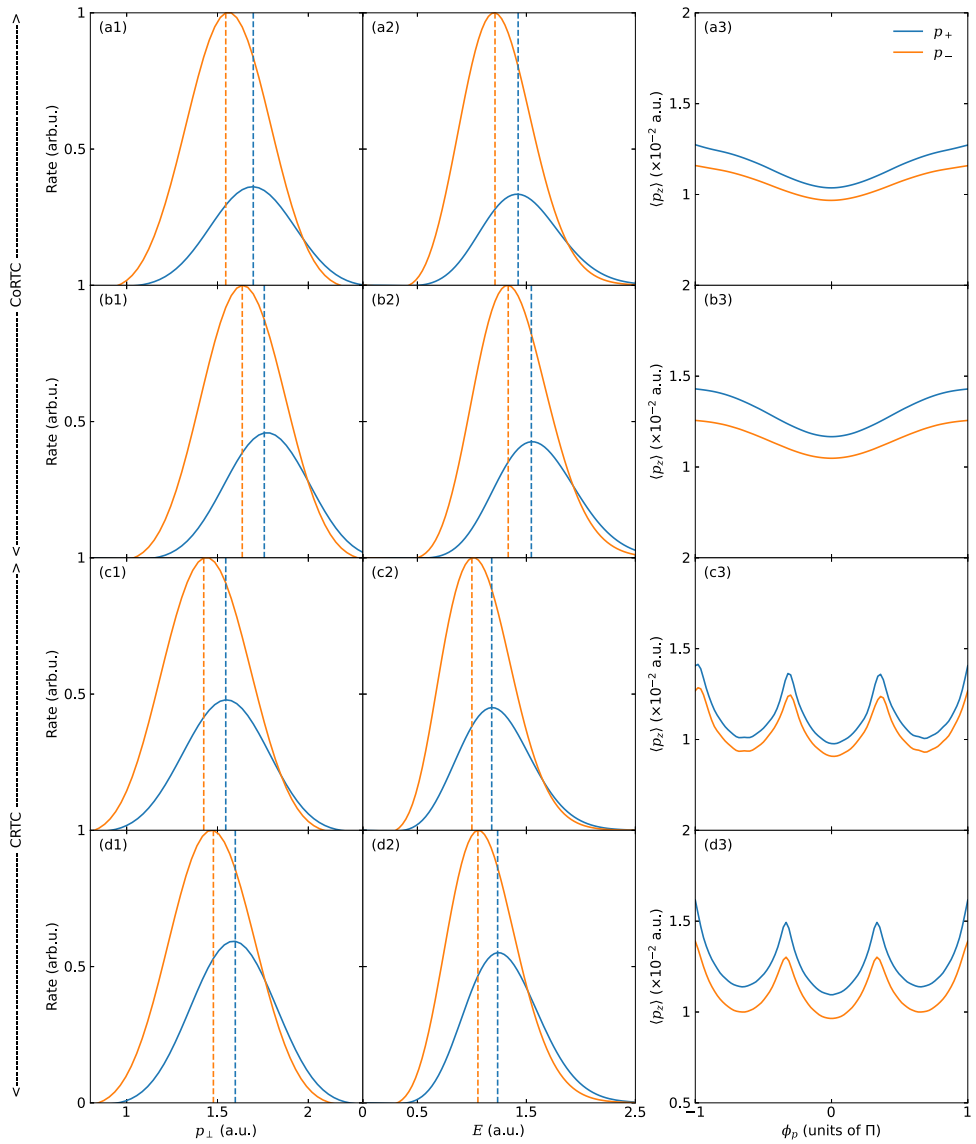

Figure 6. Same as figure 4 but for the CoRTC [the upper two rows (a) and (b)] and CRTC [the lower two rows (c) and (d)] fields. The results displayed in rows (a) and (c) are obtained from the TDSE method, whereas those in rows (b) and (d) are computed using the m-ndSPA method.

It is interesting to note that the m-ndSPA method reproduces the computational outcomes obtained from the TDSE method, including the order for $\langle p_z \rangle$ in the asymptotic region for $p_\pm$ electrons, as depicted in figure 4(b3), even though the order for $\langle v_z \rangle$ at the tunnel exit is opposite. The reason is that the continuum motion plays a much more dominant role in the linear momentum transfer compared to the quantum tunneling process.

The behavior of $p_\pm$ electrons in the EP field (Figure 5) and the TC field (Figure 6) closely resembles the dynamics found in the CP field (figure 4). In the asymptotic region, the p_+ electron demonstrates higher asymptotic radial momentum, energy, and linear momentum transfer than the p_- electron. Furthermore, it is easy to show that $A_{\mathrm{CoRTC}} > A_{\mathrm{CRTC}}$ when the electric field reaches its maximum value (see table 1), thus the asymptotic radial momentum of both p_+ and p_- electrons in the CoRTC field is greater than that in the CRTC field, as illustrated in figure 6.

Experimentally, the asymptotic momenta of p_+ and p_- electrons can be measured using a two-pulse setup [10]. First, a CP pump pulse ionizes the target. Nonadiabatic effects [8, 9] preferentially deplete electrons counter-rotating with the field, leaving a sample dominated by either p_+ or p_- electrons. A subsequent, more intense CP probe pulse then ionizes a second electron. By comparing corotating and counter-rotating pump-probe sequences, the measured yield of the second electron corresponds to the ionization of pre-selected p_+ or p_- electrons, respectively. This technique allows for the direct experimental measurement of the asymptotic average linear momentum transfer $\langle p_z \rangle$ for both p_+ and p_- electrons.

5. Conclusions

In summary, we propose a magnetic quantum number m-resolved nondipole saddle-point approximation (m-ndSPA) method to analyze the tunneling dynamics of photoelectrons from different atomic orbitals in strong CP, EP, and TC fields. We analyze the extracted linear momentum transfer characteristics. In the asymptotic region, both the TDSE method and the m-ndSPA method lead to the finding that the p_- electron (counterrotating to the field) has a lower asymptotic linear momentum transfer than the p_+ electron (corotating to the field), a conclusion that holds true for CP, EP, and TC fields. However, based on the results from the backpropagation method, the p_- electron exhibits a larger linear momentum transfer at the tunnel exit compared to the p_+ electron, which the m-ndSPA method fails to capture. This finding necessitates further refinement of the m-ndSPA method.

Additionally, all methods consistently identify the other behaviors of $p_\pm$ photoelectrons: (1) At the tunnel exit, compared to the p_+ electron, the p_- electron is ionized with a higher probability from a position closer to the nucleus. Despite having a smaller initial transverse momentum than the p_+ electron, the p_- electron possesses a larger initial energy owing to its closer initial position to the nucleus. (2) In the asymptotic region, the p_+ electron exhibits larger asymptotic radial momentum and energy relative to the p_- electron. This study enriches our understanding of the nondipole tunneling dynamics of photoelectrons from different atomic orbitals at the tunnel exit and in the asymptotic region, and, to some extent, refines the theoretical framework for the interplay between nondipole effects and magnetic quantum numbers in SFI.

Acknowledgments

This work was supported by the Quantum Science and Technology—National Science and Technology Major Project (Grant No. 2024ZD0300700), the National Natural Science Foundation of China (Grants No. 12474341, No. 12227807, and No. 12241407), the Science and Technology Commission of Shanghai Municipality (Grant No. 23JC1402000), and the Shanghai Pilot Program for Basic Research (Grant No. TQ20240204). Numerical computations were in part performed on the ECNU Multifunctional Platform for Innovation (001).

Data availability statement

The data that support the findings of this study are openly available at the following URL/DOI: https://doi.org/10.5281/zenodo.15324748.

Appendix. Comparison between m-ndSPA and m-SPA

To verify the reliability of the m-ndSPA method, we compare the photoelectron dynamics at the tunnel exit and in the asymptotic region calculated by the m-ndSPA and m-SPA methods.

Figure 7 displays the distributions of (1) initial transverse momentum, (2) energy, (3) position, and (4) the subcycle time-resolved linear momentum $\langle v_z(t_r)\rangle$ at the tunnel exit for photoelectrons ionized from $p_\pm$ orbitals of Ne in the CP field, calculated by the m-ndSPA (blue and orange solid lines) and m-SPA (green and red solid lines) methods. The results show that the initial transverse momentum, energy, and position distributions exhibit no observable differences between the dipole and the nondipole cases. This is because the nondipole contribution to the linear momentum transfer is along the laser propagation direction, which only influence the momentum distribution in the polarization plane by a high-order coupling through the Coulomb interaction that deviates from the cylindrical geometry. In addition, the nondipole effect itself is of order c^{-1}, making it difficult to distinguish nondipole results from dipole ones in the polarization plane. However, a clear distinction emerges in the average linear momentum transfer $\langle v_z\rangle$ along the laser propagation direction. While $\langle v_z\rangle = 0$ under the dipole approximation, it becomes non-zero when nondipole effects are included.

The same phenomenon is observed in the asymptotic region. In figure 8, the distributions of (1) asymptotic radial momentum and (2) energy show negligible differences between the dipole and nondipole cases, owing to minimal linear momentum transfer and its negligible coupling to the momentum distribution across the polarization plane. Along the laser propagation direction, the dipole result $\langle p_z\rangle$ is zero, while the nondipole effects result in a non-zero component.

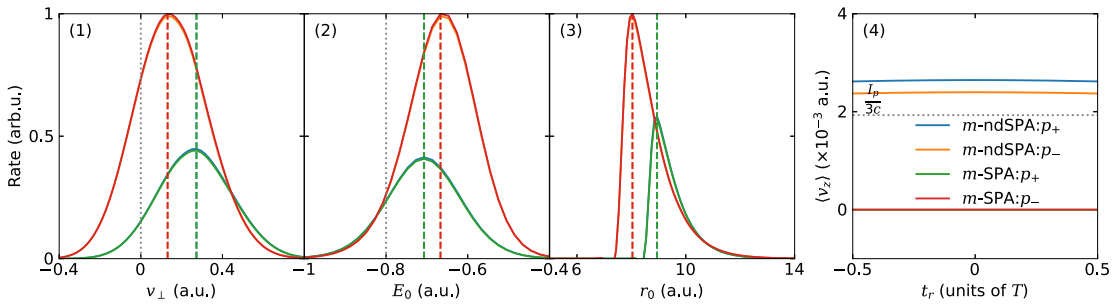

Figure 7. The distributions of initial transverse momentum [column (1)], energy [column (2)], position [column (3)], and the subcycle time-resolved linear momentum $\langle v_z \rangle(t_r)$ [column (4)] at the tunnel exit for photoelectrons ionized from $p_\pm$ orbitals of Ne in the CP field, calculated by the *m*-ndSPA (blue and orange solid lines) and *m*-SPA (green and red solid lines) methods. The blue and green solid lines correspond to the p_+ orbital, and the orange and red solid lines represent the p_- orbital, with vertical dashed lines marking their respective distribution peaks. The gray dotted lines mark the positions of $v_\perp = 0$, $E_0 = -I_p$, and $\langle v_z \rangle = I_p/(3c)$.

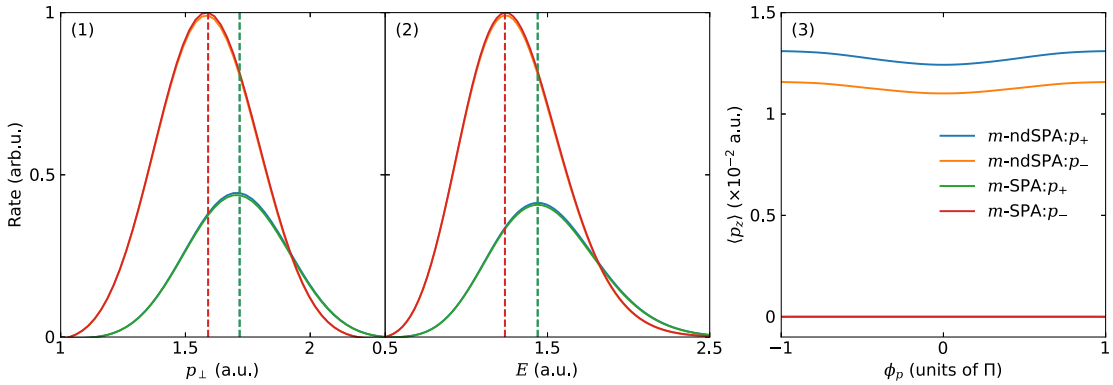

Figure 8. The distributions of asymptotic radial momentum [column (1)], energy [column (2)], and the linear momentum transfer $\langle p_z \rangle$ as a function of the attoclock angle ϕ_p [column (3)] in the asymptotic region for photoelectrons ionized from $p_\pm$ orbitals of Ne in the CP field, calculated by *m*-ndSPA (blue and orange solid lines) and *m*-SPA (green and red solid lines) methods. The blue and green solid lines correspond to the p_+ orbital, and the orange and red solid lines represent the p_- orbital, with vertical dashed lines marking their respective distribution peaks.

References

[1] Krausz F and Ivanov M 2009 Attosecond physics *Rev. Mod. Phys.* **81** 163
[2] Ma Y, Ni H and Wu J 2024 Attosecond ionization time delays in strong-field physics *Chin. Phys. B* **33** 013201
[3] Popruzhenko S 2014 Keldysh theory of strong field ionization: history, applications, difficulties and perspectives *J. Phys. B* **47** 204001
[4] Porat G *et al* 2018 Attosecond time-resolved photoelectron holography *Nat. Commun.* **9** 2805
[5] Han M, Ge P, Fang Y, Yu X, Guo Z, Ma X, Deng Y, Gong Q and Liu Y 2019 Unifying tunneling pictures of strong-field ionization with an improved attoclock *Phys. Rev. Lett.* **123** 073201
[6] Li Y, Lan P, Xie H, He M, Zhu X, Zhang Q and Lu P 2015 Nonadiabatic tunnel ionization in strong circularly polarized laser fields: counterintuitive angular shifts in the photoelectron momentum distribution *Opt. Express* **23** 28801
[7] Eckart S *et al* 2018 Ultrafast preparation and detection of ring currents in single atoms *Nat. Phys.* **14** 701
[8] Barth I and Smirnova O 2011 Nonadiabatic tunneling in circularly polarized laser fields: physical picture and calculations *Phys. Rev. A* **84** 063415
[9] Barth I and Smirnova O 2013 Nonadiabatic tunneling in circularly polarized laser fields. ii. derivation of formulas *Phys. Rev. A* **87** 013433
[10] Eckart S *et al* 2018 Ultrafast preparation and detection of ring currents in single atoms *Nat. Phys.* **14** 701
[11] Herath T, Yan L, Lee S K and Li W 2012 Strong-field ionization rate depends on the sign of the magnetic quantum number *Phys. Rev. Lett.* **109** 043004
[12] Liu K, Ni H, Renziehausen K, Rost J-M and Barth I 2018 Deformation of atomic $p_\pm$ orbitals in strong elliptically polarized laser fields: ionization time drifts and spatial photoelectron separation *Phys. Rev. Lett.* **121** 203201
[13] Ma Y, Ni H, Li Y, He F and Wu J 2024 Subcycle conservation law in strong-field ionization *Ultrafast Sci.* **4** 0071
[14] Dubois J, Lévêque C, Caillat J, Taïeb R, Saalmann U and Rost J-M 2024 Energy conservation law in strong-field photoionization by circularly polarized light *Phys. Rev. A* **109** 013112
[15] Mao X, Liu K, Ni H and Wu J 2025 Modification of the saddle-point equation for strong-field ionization from atomic *p* orbitals *Phys. Rev. A* **111** 033113
[16] Liu M-M, Li M, Shao Y, Han M, Gong Q and Liu Y 2017 Effects of orbital and coulomb potential in strong-field nonadiabatic tunneling ionization of atoms *Phys. Rev. A* **96** 043410

[17] Liu K, Li M, Xie W, Guo K, Luo S, Yan J, Zhou Y and Lu P 2020 Revealing the effect of atomic orbitals on the phase distribution of an ionizing electron wave packet with circularly polarized two-color laser fields *Opt. Express* **28** 12439
[18] Liu K, Li M, Xie W, Qin Y, Guo K, Yan J, Liu K, Zhou Y and Lu P 2022 Laser-induced deformation of atomic $p_{\pm}$ orbitals in orthogonally polarized two-color laser fields *J. Opt. Soc. Am. B* **39** 1557
[19] Wang M-X, Chen S-G, Liang H and Peng L-Y 2020 Review on non-dipole effects in ionization and harmonic generation of atoms and molecules *Chin. Phys. B* **29** 013302
[20] Maurer J and Keller U 2021 Ionization in intense laser fields beyond the electric dipole approximation: concepts, methods, achievements and future directions *J. Phys. B* **54** 094001
[21] Smeenk C, Arissian L, Zhou B, Mysyrowicz A, Villeneuve D, Staudte A and Corkum P B 2011 Partitioning of the linear photon momentum in multiphoton ionization *Phys. Rev. Lett.* **106** 193002
[22] Ludwig A, Maurer J, Mayer B, Phillips C, Gallmann L and Keller U 2014 Breakdown of the dipole approximation in strong-field ionization *Phys. Rev. Lett.* **113** 243001
[23] Hartung A *et al* 2019 Magnetic fields alter strong-field ionization *Nat. Phys.* **15** 1222
[24] Klaiber M, Yakaboylu E, Bauke H, Hatsagortsyan K Z and Keitel C H 2013 Under-the-barrier dynamics in laser-induced relativistic tunneling *Phys. Rev. Lett.* **110** 153004
[25] Chelkowski S, Bandrauk A D and Corkum P B 2014 Photon momentum sharing between an electron and an ion in photoionization: from one-photon (photoelectric effect) to multiphoton absorption *Phys. Rev. Lett.* **113** 263005
[26] Schmidt M *et al* 2024 Role of the binding energy on nondipole effects in single-photon ionization *Phys. Rev. Lett.* **132** 233002
[27] Seaton M 1995 Momentum transfer in photo-ionization processes *J. Phys. B* **28** 3185
[28] Wang M-X, Xiao X-R, Liang H, Chen S-G and Peng L-Y 2017 Photon-momentum transfer in one- and two-photon ionization of atoms *Phys. Rev. A* **96** 043414
[29] Mao X, Ni H, Gong X, Burgdörfer J and Wu J 2022 Subcycle-resolved strong-field tunneling ionization: identification of magnetic dipole and electric quadrupole effects *Phys. Rev. A* **106** 063105
[30] Hartung A *et al* 2021 Electric nondipole effect in strong-field ionization *Phys. Rev. Lett.* **126** 053202
[31] Liang H, Wang M-X, Xiao X-R, Gong Q and Peng L-Y 2018 Photon-momentum transfer in diatomic molecules: an ab initio study *Phys. Rev. A* **98** 063413
[32] He P-L, Klaiber M, Hatsagortsyan K Z and Keitel C H 2022 Nondipole coulomb sub-barrier ionization dynamics and photon momentum sharing *Phys. Rev. A* **105** L031102
[33] Klaiber M, Lv Q Z, Sukiasyan S, Bakucz Canário D, Hatsagortsyan K Z and Keitel C H 2022 Reconciling conflicting approaches for the tunneling time delay in strong field ionization *Phys. Rev. Lett.* **129** 203201
[34] Lund M M and Madsen L B 2021 Nondipole photoelectron momentum shifts in strong-field ionization with mid-infrared laser pulses of long duration *J. Phys. B* **54** 165602
[35] Brennecke S and Lein M 2021 Nondipole modification of the ac stark effect in above-threshold ionization *Phys. Rev. A* **104** L021104
[36] Kahvedžić R and Gräfe S 2022 Strong-field approximation with leading-order nondipole corrections *Phys. Rev. A* **105** 063102
[37] Della Picca R, Randazzo J M, López S D, Ciappina M F and Arbó D G 2023 Laser-assisted photoionization beyond the dipole approximation *Phys. Rev. A* **107** 053104
[38] Mao X, Ni H, Lin K, He P-L, Liang H, Eckart S, He F, Ueda K, Dörner R and Wu J 2025 Photon momentum transfer and partitioning: from one to many *Nat. Commun.* **16** 5977
[39] Lin K *et al* 2022 Photoelectron energy peaks shift against the radiation pressure in strong-field ionization *Sci. Adv.* **8** eabn7386
[40] Willenberg B, Maurer J, Mayer B W and Keller U 2019 Sub-cycle time resolution of multi-photon momentum transfer in strong-field ionization *Nat. Commun.* **10** 5548
[41] Eckle P, Smolarski M, Schlup P, Biegert J, Staudte A, Schöffler M, Muller H G, Dörner R and Keller U 2008 Attosecond angular streaking *Nat. Phys.* **4** 565
[42] Eckle P, Pfeiffer A, Cirelli C, Staudte A, Dorner R, Muller H, Buttiker M and Keller U 2008 Attosecond ionization and tunneling delay time measurements in helium *Science* **322** 1525
[43] Ni H *et al* 2020 Theory of subcycle linear momentum transfer in strong-field tunneling ionization *Phys. Rev. Lett.* **125** 073202
[44] Mao X, Ni H and Wu J 2024 Visualization of subcycle nonadiabatic-nondipole coupling in strong-field ionization *Phys. Rev. A* **110** 063113
[45] Klünder K *et al* 2011 Probing single-photon ionization on the attosecond time scale *Phys. Rev. Lett.* **106** 143002
[46] Liang J, Han M, Liao Y, Ji J-b, Leung C S, Jiang W-C, Ueda K, Zhou Y, Lu P and Wörner H J 2024 Attosecond-resolved non-dipole photoionization dynamics *Nat. Photonics* **18** 311
[47] Brennecke S and Lein M 2018 High-order above-threshold ionization beyond the electric dipole approximation *J. Phys. B* **51** 094005
[48] Sun F *et al* 2020 Longitudinal photon-momentum transfer in strong-field double ionization of argon atoms *Phys. Rev. A* **101** 021402
[49] Lin K *et al* 2022 Magnetic-field effect in high-order above-threshold ionization *Phys. Rev. Lett.* **128** 023201
[50] Liao Y, Chen Y, Dahlström J M, Pi L-W, Lu P and Zhou Y 2024 Linearly polarized rabbit beyond the dipole approximation *Phys. Rev. A* **110** 023109
[51] Dou Y, Long X, Li P, Ge P, Deng Y, Gong Q and Liu Y 2025 Controlling nondipole effects with bicircular laser fields *Phys. Rev. A* **111** 013114
[52] Jašarević A, Habibović D and Milošević D 2024 Quantum orbits in atomic ionization beyond the dipole approximation *Phys. Rev. A* **110** 023111
[53] Eicke N, Brennecke S and Lein M 2020 Attosecond-scale streaking methods for strong-field ionization by tailored fields *Phys. Rev. Lett.* **124** 043202
[54] Ni H, Saalmann U and Rost J-M 2016 Tunneling ionization time resolved by backpropagation *Phys. Rev. Lett.* **117** 023002
[55] Ni H, Saalmann U and Rost J-M 2018 Tunneling exit characteristics from classical backpropagation of an ionized electron wave packet *Phys. Rev. A* **97** 013426
[56] Ni H, Eicke N, Ruiz C, Cai J, Oppermann F, Shvetsov-Shilovski N I and Pi L-W 2018 Tunneling criteria and a nonadiabatic term for strong-field ionization *Phys. Rev. A* **98** 013411
[57] He P-L, Lao D and He F 2017 Strong field theories beyond dipole approximations in nonrelativistic regimes *Phys. Rev. Lett.* **118** 163203
[58] Kylstra N J, Potvliege R and Joachain C 2001 Photon emission by ions interacting with short intense laser pulses: beyond the dipole approximation *J. Phys. B* **34** L55
[59] Wang J-P and He F 2017 Tunneling ionization of neon atoms carrying different orbital angular momenta in strong laser fields *Phys. Rev. A* **95** 043420

[60] Zhang Q, Basnayake G, Winney A, Lin Y F, Debrah D, Lee S K and Li W 2017 Orbital-resolved nonadiabatic tunneling ionization *Phys. Rev. A* **96** 023422
[61] Kim Y H, Ivanov I A and Kim K T 2021 Classical backpropagation for probing the backward rescattering time of a tunnel-ionized electron in an intense laser field *Phys. Rev. A* **104** 013116
[62] Gribakin G and Kuchiev M Y 1997 Multiphoton detachment of electrons from negative ions *Phys. Rev. A* **55** 3760
[63] Jašarević A, Hasović E, Kopold R, Becker W and Milošević D 2020 Application of the saddle-point method to strong-laser-field ionization *J. Phys. A* **53** 125201
[64] Ma Y, Zhou J, Lu P, Ni H and Wu J 2021 Influence of nonadiabatic, nondipole and quantum effects on the attoclock signal *J. Phys. B* **54** 144001